A&A 518, L30 (2010)
DOI: 10.1051/0004-6361/201014610

Astronomy & Astrophysics
Special feature

Herschel: the first science highlights

Letter to the Editor

Dissecting the cosmic infra-red background with *Herschel*/PEP⋆,⋆⋆

S. Berta[1], B. Magnelli[1], D. Lutz[1], B. Altieri[2], H. Aussel[3], P. Andreani[4,5], O. Bauer[1], A. Bongiovanni[6,7], A. Cava[6,7], J. Cepa[6,7], A. Cimatti[8], E. Daddi[3], H. Dominguez[9], D. Elbaz[3], H. Feuchtgruber[1], N. M. Förster Schreiber[1], R. Genzel[1], C. Gruppioni[9], R. Katterloher[1], G. Magdis[3], R. Maiolino[10], R. Nordon[1], A. M. Pérez García[6,7], A. Poglitsch[1], P. Popesso[1], F. Pozzi[8], L. Riguccini[3], G. Rodighiero[11], A. Saintonge[1], P. Santini[10], M. Sanchez-Portal[2], L. Shao[1], E. Sturm[1], L. J. Tacconi[1], I. Valtchanov[2], M. Wetzstein[1], and E. Wieprecht[1]

(Affiliations are available in the online edition)

Received 31 March 2010 / Accepted 21 April 2010

ABSTRACT

The constituents of the cosmic IR background (CIB) are studied at its peak wavelengths (100 and 160 μm) by exploiting *Herschel*/PACS observations of the GOODS-N, Lockman Hole, and COSMOS fields in the PACS evolutionary probe (PEP) guaranteed-time survey. The GOODS-N data reach 3σ depths of ~3.0 mJy at 100 μm and ~5.7 mJy at 160 μm. At these levels, source densities are 40 and 18 beams/source, respectively, thus hitting the confusion limit at 160 μm. Differential number counts extend from a few mJy up to 100-200 mJy, and are approximated as a double power law, with the break lying between 5 and 10 mJy. The available ancillary information allows us to split number counts into redshift bins. At $z \leq 0.5$ we isolate a class of luminous sources ($L_{\rm IR} \sim 10^{11}\ L_{\odot}$), whose SEDs resemble late-spiral galaxies, peaking at ~130 μm restframe and significantly colder than what is expected on the basis of pre-*Herschel* models. By integrating number counts over the whole covered flux range, we obtain a surface brightness of 6.36 ± 1.67 and 6.58 ± 1.62 [nW m^{-2} sr^{-1}] at 100 and 160 μm, resolving ~45% and ~52% of the CIB, respectively. When stacking 24 μm sources, the inferred CIB lies within 1.1σ and 0.5σ from direct measurements in the two bands, and fractions increase to 50% and 75%. Most of this resolved CIB fraction was radiated at $z \leq 1.0$, with 160 μm sources found at higher redshift than 100 μm ones.

Key words. infrared: diffuse background – infrared: galaxies – cosmic background radiation – galaxies: statistics – galaxies: evolution

1. Introduction

The cosmic IR background (CIB, Puget et al. 1996; Hauser et al. 1998) accounts for roughly half of the total extragalactic background light (EBL, Hauser & Dwek 2001; Lagache et al. 2005), i.e., half of the energy radiated by all galaxies, at all cosmic epochs, at any wavelength (Dole et al. 2006). It is therefore a crucial constraint on modes and times of galaxy formation.

Deep cosmological surveys carried out with the ISO (see Genzel & Cesarsky 2000, for a summary) and *Spitzer* Space Observatory (Soifer et al. 2008, for a review) produced large samples of mid-IR sources and deep number counts (Elbaz et al. 2002; Papovich et al. 2004). These surveys led to mid-IR CIB lower limits within a factor of two from the upper constraints set by TeV cosmic opacity measurements (e.g. Franceschini et al. 2010).

However, at CIB peak wavelengths (100–200 μm), the nature of individual galaxies building up the EBL is poorly known. Past surveys produced limited samples of distant far-IR objects (e.g. Frayer et al. 2009), mainly due to the small apertures of the available instruments and the low sensitivity in the far-IR. In the 160 μm *Spitzer*/MIPS band, ~7% of the CIB was resolved into individually detected objects (Dole et al. 2004), and it was only through stacking the 24 μm sources that most (60–70%) of the far-IR CIB could be recovered (Dole et al. 2006; Béthermin et al. 2010). Similarly, at longer wavelengths, only stacking of 24 μm sources on BLAST maps could account for the majority of the EBL at 250, 350, and 500 μm (Marsden et al. 2009).

With the favorable diffraction limit of the large *Herschel* 3.5 m mirror (Pilbratt et al. 2010), and the high sensitivity of its Photodetector Array Camera and Spectrometer (PACS, 70, 100, 160 μm; Poglitsch et al. 2010), confusion and blending of sources are much less of a limitation. We are now able to resolve a large fraction of the CIB at its peak into individual galaxies.

The PACS evolutionary probe (PEP) extragalactic survey samples 4 different tiers: from the wide and shallow COSMOS field, through medium size areas like the Lockman hole, all the way down to the 160 and 100 μm confusion limit in the pencil-beam, very deep observations in GOODS-N and GOODS-S, and even beyond by exploiting gravitational lensing in low-redshift galaxy clusters (e.g. Abell 2218; Altieri et al. 2010).

Here we exploit the science demonstration phase (SDP) observations of the GOODS-N field, complemented with the COSMOS and Lockman hole (LH) wider and shallower layers of the survey, to build far-IR galaxy number counts and derive the fraction of CIB resolved by PEP. We then take advantage of the extensive multi-wavelength coverage of the GOODS-N field, with the aim of identifying the CIB contributors and the epoch when the bulk of the Universe IR energy budget was emitted.

2. Number counts

The area used to derive number counts includes observations in the GOODS-N (~140 arcmin^2), COSMOS (~2 deg^2) and LH

⋆ *Herschel* is an ESA space observatory with science instruments provided by European-led Principal Investigator consortia and with important participation from NASA.

⋆⋆ Table 1 and Appendix A are only available in electronic form at http://www.aanda.org

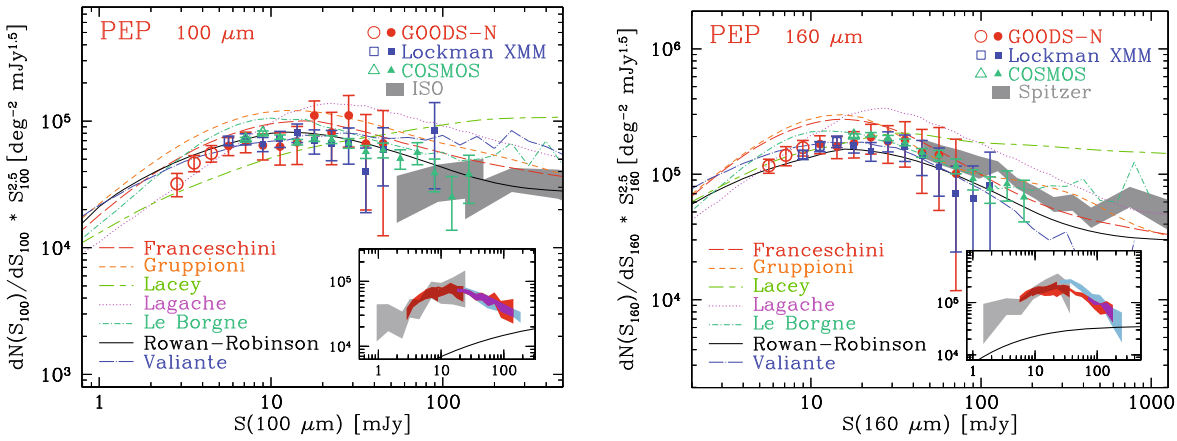

Fig. 1. Number counts at 100 (*left*) and 160 μm (*right*), normalized to the Euclidean slope. Filled/open symbols belong to flux bins above/below the 80% completeness limit. Models belong to Lagache et al. (2004), Franceschini et al. (2010), Rowan-Robinson (2009), Le Borgne et al. (2009), Valiante et al. (2009), Lacey et al. (2010), Gruppioni & Pozzi (in prep.). Shaded areas represent ISO and *Spitzer* data (Rodighiero & Franceschini 2004; Héraudeau et al. 2004; Béthermin et al. 2010). *Inset*: Collection of PACS number counts, including this work (red, limited to relative errors ≤15% for clarity sake), PEP Abell 2218 (grey, Altieri et al. 2010) and HerMES-PACS (light-blue, Aussel et al., in prep.). The solid lines in the insets mark the trends expected for a non-evolving population of galaxies.

(~450 arcmin^2) fields. Appendix A describes data reduction and catalog extraction.

PACS number counts were computed in each field within 0.1 dex flux bins, and are reported in Fig. 1 and Table 1, normalized to the Euclidean slope ($dN/dS \propto S^{-2.5}$). Incompleteness and spurious sources have been dealt with using Monte Carlo simulations (see Appendix A). Filled symbols belong to the conservative 80% completeness limit. Thanks to the method described in Chary et al. (2004), we extend the analysis down to the faintest objects detected at the 3σ level. Error bars include Poisson statistics, flux calibration uncertainties, and photometric errors. The latter have been propagated into number counts via 10^4 realizations of random Gaussian flux errors applied to each PACS source, using a dispersion equal to the local measured noise. The 95 μm ISO counts (Rodighiero & Franceschini 2004; Héraudeau et al. 2004) and the 160 μm *Spitzer* results by Béthermin et al. (2010, including GOODS/FIDEL, COSMOS and SWIRE fields) are consistent with PACS data, excepted the ISO faintest flux bin.

Small insets in Fig. 1 show results from PACS guaranteed-time surveys: this work, Abell 2218 lensed counts (Altieri et al. 2010), and HerMES (Aussel et al., in prep.). The three datasets complement each other and show overall agreement, the 160 μm HerMES counts excepted. This discrepancy can be ascribed to the sheet of galaxies known to bias the HerMES LH *North* field, on which their counts are based (Owen & Morrison 2009).

Differential, Euclidean-normalized counts display various well-known features: below ~100 mJy at 100 μm and ~200 mJy at 160 μm, the slope is super-Euclidean, reaching a peak in the counts between ~5–10 and 30 mJy, while at fainter fluxes the slope quickly becomes sub-Euclidean. These attributes are generally interpreted as indicating evolving properties in the IR galaxy population (see Sect. 4): the trend expected for no-evolution is shown in Fig. 1 insets.

The non-normalized differential counts can be represented by a power law of the type $dN/dS \propto S^{\alpha}$, with two distinct slopes at fluxes fainter/brighter than $S_{\rm break}$. The results of a weighted least squares fit are given in Table 2 for the different PEP fields. The $S_{\rm break}$ flux is ~5.0 mJy at 100 μm and ~8.5 mJy at 160 μm. At the bright end, the number of sources in the small fields is low, and error bars are dominated by Poisson statistics. Consequently, the large uncertainties allow for nearly-Euclidean fits in GOODS-N and the LH. In the case of COSMOS, the slope is significantly steeper than Euclidean at 160 μm, while the 100 μm counts are still very flat. At the faint end, the 160 μm slope derived from our counts (GOODS-N only) is consistent with what is found by stacking 24 μm sources on *Spitzer* 160 μm maps (Béthermin et al. 2010, $\alpha = -1.61 \pm 0.21$).

Table 2. Power-law fit to PACS differential number counts in the form $dN/dS \propto S^{\alpha}$.

Field band	Flux range [mJy]	Slope α	Error $d\alpha$
GOODS-N 100	2.8–5.6	–1.32	±0.27
GOODS-N 100	5.6–45	–2.31	±0.05
LH 100	6.0–89	–2.60	±0.05
COSMOS 100	8.0–142	–2.63	±0.03
GOODS-N 160	5.6–9.0	–1.67	±0.32
GOODS-N 160	9.0–71	–2.54	±0.04
LH 160	9.0–113	–2.68	±0.05
COSMOS 160	17.0–179	–3.02	±0.04

3. Resolved CIB fraction

The added contribution of resolved galaxies provides a lower limit to the IR background and can be compared to direct measurements of the total CIB. After the discovery of the CIB (Puget et al. 1996; Hauser et al. 1998), numerous authors attempted to directly measure its surface brightness from COBE/DIRBE maps (e.g. Lagache et al. 2000; Renault et al. 2001; Wright 2004; Dole et al. 2006). Here we adopt the most recent revision of the Lagache et al. (2000) DIRBE measurements, provided in Dole et al. (2006): 14.4 ± 6.3, 12.0 ± 6.9, and 12.3 ± 2.5 [nW m^{-2} sr^{-1}], at 100, 140, and 240 μm, respectively. Interpolating between these values, one obtains a value of 12.8 ± 6.4 [nW m^{-2} sr^{-1}] at 160 μm. These direct measurements are still affected by large uncertainties, mainly due to difficulties in defining an absolute flux scale and in removing zodiacal light. An alternative estimate of the total CIB is obtained by integrating the power-law extrapolation of our number counts, between 0.01 and 1000 mJy. We adopt the slope derived on GOODS-N data for $S < S_{\rm break}$ and an average between COSMOS and Lockman Hole at brighter fluxes (see Table 2 and Sect. 2). The total CIB estimates from this extrapolation are ~12 and ~13 [nW m^{-2} sr^{-1}] in the green

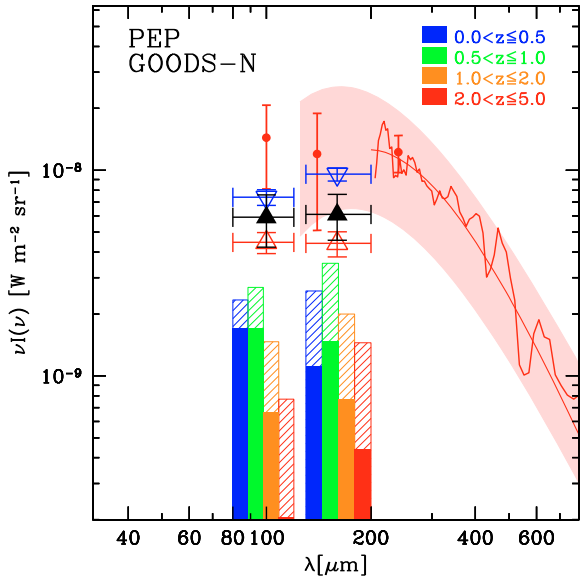

Fig. 2. Contribution of GOODS-N galaxies to the CIB. Red empty triangles represent the sum of individually detected sources; black filled triangles come from number counts above the 3σ limit, and include completeness correction; blue upside-down empty triangles belong to stacking of 24 μm sources. Solid histograms denote the contribution of different redshift bins to the CIB, accounting for completeness correction. Hatched histograms are stacking results. Literature data include: DIRBE measurements revised by Dole et al. (2006, filled circles, 1σ errors); FIRAS spectrum (solid lines above 200 μm, Lagache et al. 1999, 2000); Fixsen et al. (1998) modified Black Body (shaded area).

(100 μm) and red (160 μm) bands, within the errors of the direct measurements.

The contribution to the CIB of individual GOODS-N sources detected above 3σ is $\nu I_\nu = 4.46 \pm 0.52$ at 100 μm and 4.41 ± 0.62 [nW m^{-2} sr^{-1}] at 160 μm, i.e., $\sim 31 \pm 4\%$ and $\sim 35 \pm 5\%$ of the direct DIRBE measurements (Fig. 2). Taking the effects of completeness into account (see Sect. 2), we can compute the CIB fraction due to the general FIR-population, overriding source extraction losses. We limit the analysis to the 3σ detection limit again. The GOODS-N number counts cover the ranges 3–45 mJy (at 100 μm) and 5.5–72 mJy (at 160 μm); the COSMOS field allows upper boundaries to be extended to 142 and 179 mJy. Integrating the counts over the whole flux range, we obtain $\nu I_\nu = 6.36 \pm 1.67$ and 6.58 ± 1.62 [nW m^{-2} sr^{-1}], within 1.3σ and 1.0σ from the reference values at 100 and 160 μm, respectively (Fig. 2). These correspond to $\sim 45 \pm 12\%$ and $\sim 52 \pm 13\%$ of the Dole et al. (2006) estimate. The derived uncertainty now also includes the effect of Poisson statistics and not only photometric errors. The bright end of number counts, covered only by COSMOS, gives a small contribution ($\sim$4–6%) to the total CIB surface brightness.

The PACS detection rate of *Spitzer* 24 μm sources ($S_{24} \geq 20$ μJy, Magnelli et al. 2009) is roughly 15%. It is possible to derive a deeper CIB estimate, through stacking on the PEP maps at the positions of all 24 μm objects, including those not detected in the FIR (e.g. Dole et al. 2006). Uncertainties on the stacked fluxes are computed via a simple bootstrap procedure. The CIB surface brightness produced by 24 μm sources is 7.39 ± 0.48 and 9.57 ± 0.71 [nW m^{-2} sr^{-1}] at 100 and 160 μm, consistent with Béthermin et al. (2010), and providing $\sim$51% and $\sim$75% of the total background, within 1.1σ and 0.5σ from Dole et al. (2006).

4. Discussion

In the attempt to reproduce the observed ISO and *Spitzer* number counts, several authors built "backward" evolutionary models, including luminosity and/or density evolution, as well as different galaxy populations. In Fig. 1, we overlay recent models onto the observed PACS counts. We include in this collection the Lacey et al. (2010) Λ-CDM semi-analytical model (SAM), complemented with radiative transfer dust reprocessing. The most successful models are the Valiante et al. (2009), including luminosity-dependent distribution functions for the galaxy IR SEDs and their AGN contribution, and Rowan-Robinson (2009), employing analytic evolutionary functions without discontinuities and 4 galaxy populations.

Gruppioni and Lagache et al. (2004) overestimate the amplitude of the number counts peak in both bands, while Franceschini et al. (2010) and Le Borgne et al. (2009) reproduce the counts fairly well only in one channel (100 and 160 μm, respectively). It is worth recalling that to date most of these models have been fine-tuned to reproduce mid-IR and sub-mm statistics, while a big gap in wavelength was affecting far-IR predictions. Most include a luminosity evolution $\propto (1+z)^{3.0-3.5}$, but the redshift limit for this slope, the details of density evolution, or the adopted galaxy zoo vary significantly from author to author.

Besides spanning a much wider range of observational data (UV, optical, near-IR luminosity functions, galaxy sizes, metallicity, etc.), the SAM approach suffers here for a limited flexibility in the choice of parameters, and significantly overestimates the bright end of PACS counts. Moreover, it cannot reproduce the peak, especially in the green band.

Thanks to the rich ancillary dataset in GOODS-N, we split the far-IR number counts into redshift bins (Fig. 3). This elaboration offers a remarkable chance to set detailed constraints on the evolution of the galaxy populations adopted in current recipes. This view highlights some new features and the main problems of the models under discussion.

First, in the lowest redshift bin, $0.0 < z \leq 0.5$, the differential number counts, normalized to the Euclidean slope, monotonically increase as a function of flux, resembling the trend expected for a non-evolving population of galaxies. The consistency of models with data weakens at longer wavelengths. At the bright end, above 10 mJy and 20 mJy at 160 μm, PEP catalogs include 43 and 18 objects in this redshift range. Based on template fitting (Rodighiero et al. 2010), half of this sample shows a late-spiral SED (*Sd-Sdm* in the Polletta et al. 2007, template library) with typical luminosities above 10^{11} $L_\odot$ and a peak wavelength of $\sim$130 μm. Nevertheless, at these luminosities, Chary & Elbaz (2001) models, which adopt the local $L-T$ relation, predict SEDs peaking around 90 μm restframe, thus indicating that this class is indeed colder than typical local IR-luminous sources. This is reminiscent of the cold sources found by ISO FIRBACK and serendipity surveys (e.g. Dennefeld et al. 2005; Stickel et al. 2007).

Significant differences between models arise at higher redshift. The bin $1.0 < z \leq 2.0$ shows the largest discrepancies: apparently, most of the overestimation of total number counts by some models originates here, suggesting that the adopted evolution is either too protracted in time or too steep.

We are now able for the first time to infer how much of the resolved CIB peak was emitted at different cosmic epochs. Figure 2 depicts the amount of extragalactic IR background originating from the four redshift bins taken into account (see also Fig. 3). At 100 μm, at the GOODS-N 3σ limit of $\sim$3 mJy, roughly 80% of the resolved CIB is emitted by objects detected

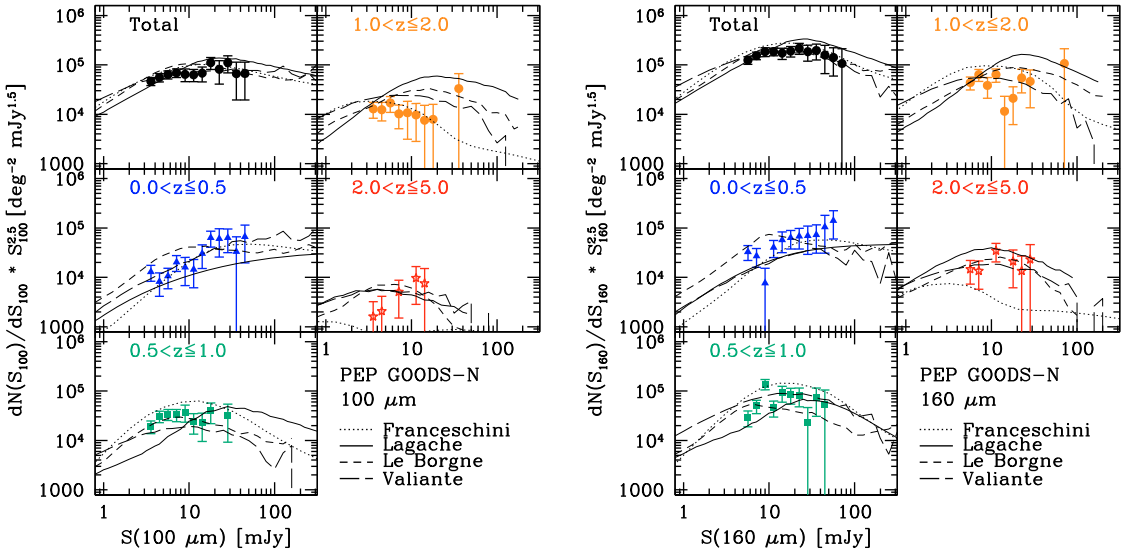

Fig. 3. Slicing the PEP GOODS-N population into redshift bins. Each PACS source has been associated to an optical/mid-IR counterpart as described in Appendix A. See Fig. 1 and text for details on the models shown.

at $z \leq 1$, equally distributed below and above $z = 0.5$. The remainder belongs to more distant galaxies, with only 5% locked into individual objects at $z > 2$. Most of the resolved 160 μm CIB is produced at higher redshift, with the $0.5 < z \leq 1.0$ redshift bin dominating (~40%) the budget.

At the PEP depth, the CIB resolved into individual sources is mainly due to luminous and ultraluminous IR galaxies (LIRGs $10^{11} \leq L_{\rm IR} < 10^{12}\ L_{\odot}$, ULIRGs $L_{\rm IR} \geq 10^{12}\ L_{\odot}$). The relative fraction of the two classes varies as a function of redshift, likely due to selection effects, with LIRGs providing 80–90% of the CIB resolved at $0.5 < z \leq 1$ and ULIRGs dominating at higher redshift (60–70% at $1.0 < z \leq 2.0$ and 100% above).

Finally, Fig. 2 also reports the CIB contribution of 24 μm sources, as obtained through stacking (see Sect. 3). The relative CIB fractions emitted in the four redshift bins change significantly at 100 μm, with respect to those obtained by integrating the observed counts. The redshift distribution of the CIB is now peaking between $0.5 < z \leq 1.0$ and the relative contribution of $z > 1$ increases by more than 10%. On the other hand, at 160 μm only the relative fraction of the highest redshift bin varies by more than 5%, while the others remain unchanged within 1–2%. Also in the case of stacking, the 160 μm CIB relative redshift distribution is more populated at high redshift than the 100 μm one. As expected, this indicates that PACS galaxies with redder observed colors lie on average at higher redshift than bluer ones.

Acknowledgements. PACS has been developed by a consortium of institutes led by MPE (Germany) and including UVIE (Austria); KU Leuven, CSL, IMEC (Belgium); CEA, LAM (France); MPIA (Germany); INAF-IFSI/OAA/OAP/OAT, LENS, SISSA (Italy); IAC (Spain). This development has been supported by the funding agencies BMVIT (Austria), ESA-PRODEX (Belgium), CEA/CNES (France), DLR (Germany), ASI/INAF (Italy), and CICYT/MCYT (Spain).

References

Altieri, B., et al. 2010, A&A, 518, L17
Barger, A. J., Cowie, L. L., & Wang, W. 2008, ApJ, 689, 687
Béthermin, M., Dole, H., Beelen, A., & Aussel, H. 2010, A&A, 512, A78
Brammer, G. B., van Dokkum, P. G., & Coppi, P. 2008, ApJ, 686, 1503
Chary, R., & Elbaz, D. 2001, ApJ, 556, 562
Chary, R., Casertano, S., Dickinson, M. E., et al. 2004, ApJS, 154, 80
Dennefeld, M., Lagache, G., Mei, S., et al. 2005, A&A, 440, 5
Diolaiti, E., Bendinelli, O., Bonaccini, D., et al. 2000, A&AS, 147, 335
Dole, H., Lagache, G., & Puget, J. 2003, ApJ, 585, 617
Dole, H., Le Floc'h, E., Pérez-González, P. G., et al. 2004, ApJS, 154, 87
Dole, H., Lagache, G., Puget, J., et al. 2006, A&A, 451, 417
Elbaz, D., Cesarsky, C. J., Chanial, P., et al. 2002, A&A, 384, 848
Fixsen, D., Dwek, E., Mather, J., Bennett, C., & Shafer, R. 1998, ApJ, 508, 123
Franceschini, A., Rodighiero, G., Vaccari, M., et al. 2010, A&A, in press [arXiv:0906.4264]
Frayer, D. T., Sanders, D. B., Surace, J. A., et al. 2009, AJ, 138, 1261
Fruchter, A. S., & Hook, R. N. 2002, PASP, 114, 144
Genzel, R., & Cesarsky, C. J. 2000, ARA&A, 38, 761
Giavalisco, M., Ferguson, H. C., Koekemoer, A. M., et al. 2004, ApJ, 600, L93
Grazian, A., Fontana, A., de Santis, C., et al. 2006, A&A, 449, 951
Hauser, M. G., & Dwek, E. 2001, ARA&A, 39, 249
Hauser, M. G., Arendt, R. G., Kelsall, T., et al. 1998, ApJ, 508, 25
Héraudeau, P., Oliver, S., del Burgo, C., et al. 2004, MNRAS, 354, 924
Lacey, C. G., Baugh, C. M., Frenk, C. S., et al. 2010, MNRAS, 405, 2
Lagache, G., Abergel, A., Boulanger, F., Désert, & Puget. 1999, A&A, 344, 322
Lagache, G., Haffner, L., Reynolds, R., & Tufte, S. 2000, A&A, 354, 247
Lagache, G., Dole, H., & Puget, J. 2003, MNRAS, 338, 555
Lagache, G., Dole, H., Puget, J., et al. 2004, ApJS, 154, 112
Lagache, G., Puget, J., & Dole, H. 2005, ARA&A, 43, 727
Le Borgne, D., Elbaz, D., Ocvirk, P., & Pichon, C. 2009, A&A, 504, 727
Magnelli, B., Elbaz, D., Chary, R. R., et al. 2009, A&A, 496, 57
Marsden, G., Ade, P. A. R., Bock, J. J., et al. 2009, ApJ, 707, 1729
Ott, S., et al. 2010, ASP Conf Series, ADASS XIX, Mizumoto et al. eds, in press
Owen, F. N., & Morrison, G. E. 2009, ApJS, 182, 625
Papovich, C., Dole, H., Egami, E., et al. 2004, ApJS, 154, 70
Pilbratt, G. L., et al. 2010, A&A, 518, L1
Poglitsch, A., et al. 2010, A&A, 518, L2
Polletta, M., Tajer, M., Maraschi, L., et al. 2007, ApJ, 663, 81
Puget, J., Abergel, A., Bernard, J., et al. 1996, A&A, 308, L5
Renault, C., Barrau, A., Lagache, G., & Puget, J. 2001, A&A, 371, 771
Rodighiero, G., & Franceschini, A. 2004, A&A, 419, L55
Rodighiero, G., et al. 2010, A&A, 518, L25
Rowan-Robinson, M. 2009, MNRAS, 394, 117
Soifer, B. T., Helou, G., & Werner, M. 2008, ARA&A, 46, 201
Starck, J., & Murtagh, F. 1998, PASP, 110, 193
Stickel, M., Klaas, U., & Lemke, D. 2007, A&A, 466, 831
Sutherland, W., & Saunders, W. 1992, MNRAS, 259, 413
Valiante, E., Lutz, D., Sturm, E., Genzel, R., & Chapin, E. 2009, ApJ, 701, 1814
Wright, E. L. 2004, New Astron. Rev., 48, 465

Pages 5 to 7 are available in the electronic edition of the journal at http://www.aanda.org

[1] Max-Planck-Institut für Extraterrestrische Physik (MPE), Postfach 1312, 85741 Garching, Germany
e-mail: berta@mpe.mpg.de
[2] *Herschel* Science Centre, ESAC, Villanueva de la Cañada, 28691 Madrid, Spain
[3] Laboratoire AIM, CEA/DSM-CNRS-Université Paris Diderot, IRFU/Service d'Astrophysique, Bât. 709, CEA-Saclay, 91191 Gif-sur-Yvette Cedex, France
[4] ESO, Karl-Schwarzschild-Str. 2, 85748 Garching, Germany
[5] INAF – Osservatorio Astronomico di Trieste, via Tiepolo 11, 34143 Trieste, Italy
[6] Instituto de Astrofísica de Canarias, 38205 La Laguna, Spain
[7] Departamento de Astrofísica, Universidad de La Laguna, Spain
[8] Dipartimento di Astronomia, Università di Bologna, via Ranzani 1, 40127 Bologna, Italy
[9] INAF – Osservatorio Astronomico di Bologna, via Ranzani 1, 40127 Bologna, Italy
[10] INAF – Osservatorio Astronomico di Roma, via di Frascati 33, 00040 Monte Porzio Catone, Italy
[11] Dipartimento di Astronomia, Università di Padova, Vicolo dell'Osservatorio 3, 35122 Padova, Italy

Table 1. PEP number counts, normalized to the Euclidean slope.

$S_{\rm center}$	GOODS-N 100 μm		LH 100 μm		COSMOS 100 μm		GOODS-N 160 μm		LH 160 μm		COSMOS 160 μm	
2.84	3.19e+04	0.208	–	–	–	–	–	–	–	–	–	–
3.57	4.67e+04	0.146	–	–	–	–	–	–	–	–	–	–
4.50	5.57e+04	0.149	–	–	–	–	–	–	–	–	–	–
5.66	6.37e+04	0.162	7.00e+04	0.086	–	–	1.17e+05	0.129	–	–	–	–
7.13	6.90e+04	0.185	7.22e+04	0.100	7.23e+04	0.028	1.42e+05	0.173	–	–	–	–
8.97	6.43e+04	0.234	6.58e+04	0.128	8.10e+04	0.031	1.63e+05	0.142	1.43e+05	0.086	–	–
11.30	6.29e+04	0.287	7.24e+04	0.146	7.47e+04	0.039	1.74e+05	0.163	1.67e+05	0.093	–	–
14.22	6.81e+04	0.333	8.13e+04	0.167	6.81e+04	0.050	1.66e+05	0.200	1.82e+05	0.106	–	–
17.91	1.11e+05	0.302	7.00e+04	0.217	7.33e+04	0.057	1.77e+05	0.237	1.70e+05	0.132	2.03e+05	0.033
22.54	8.13e+04	0.443	6.66e+04	0.269	7.15e+04	0.071	1.97e+05	0.266	1.53e+05	0.171	2.07e+05	0.039
28.38	1.11e+05	0.438	6.70e+04	0.317	6.70e+04	0.087	1.83e+05	0.334	1.85e+05	0.183	1.95e+05	0.049
35.73	6.63e+04	0.701	4.01e+04	0.529	5.74e+04	0.116	1.88e+05	0.394	1.66e+05	0.238	1.80e+05	0.062
44.98	6.68e+04	0.814	5.97e+04	0.484	5.91e+04	0.135	1.49e+05	0.527	1.42e+05	0.312	1.48e+05	0.082
56.62	–	–	≤1.81e+04	1.000	5.06e+04	0.175	1.44e+05	0.641	1.14e+05	0.415	1.41e+05	0.100
71.29	–	–	≤2.40e+04	1.000	5.64e+04	0.198	1.01e+05	0.883	7.01e+04	0.658	1.16e+05	0.135
89.74	–	–	8.46e+04	0.655	3.89e+04	0.289	–	–	6.37e+04	0.828	9.19e+04	0.185
112.98	–	–	–	–	2.51e+04	0.453	–	–	8.19e+04	0.833	7.70e+04	0.239
142.23	–	–	–	–	3.81e+04	0.412	–	–	–	–	8.38e+04	0.271
179.06	–	–	–	–	–	–	–	–	–	–	6.57e+04	0.366

Notes. Fluxes are provided in [mJy]. For each field/wavelength, we list counts in units of [deg^{-2} mJy$^{1.5}$]. Errors are given as relative fractions, and include both Poisson statistics and propagation of photometric uncertainties.

Appendix A: PACS data

PEP science demonstration data include the GOODS-N and Abell 2218 fields. In addition to these, part of the other PEP blank fields have already been scheduled and observed: Lockman Hole and COSMOS (~85% of the planned depth). Observations of all fields were carried out by adopting the intermediate speed (20 arcsec/s) scan-map mode. Table A.1 lists the total exposure times already observed for these fields[1].

Data have been processed through the standard PACS reduction pipeline, version 2.0.1328, within the HCSS environment[2] (Ott et al. 2010). Additionally, we employed custom procedures aimed at removing of interference patterns, tracking anomalies, re-centering positional offsets, and mapping.

Glitch removal is based on *multi-resolution median transform*, developed by Starck & Murtagh (1998) to detect faint sources in ISOCAM data. The signal due to real sources and glitches show different signatures in the pixel timeline. These features are recognized using a multi-scale transform, separating the various frequencies of the signal. Once the glitch components are identified, they are replaced by interpolated values in the pixel timeline.

PACS photometers exhibit a noise with a roughly $f^{-0.5}$ spectrum at relevant frequencies. To remove the bulk of the noise we apply a "running-box" high-pass median filter to each pixel timeline, but mask the position of bright sources. The objects mask is produced iteratively during the reduction by detecting sources on the final map, and then we mask them in a double-pass mapping scheme. Testing shows that this masked filtering method modifies the fluxes of point-like source by less than 5%.

Imperfections, drifts, and errors in the pointing accuracy of the *Herschel* satellite were corrected by re-centering the data on a grid of known 24 μm sources populating the fields. Such objects were stacked for all scan-legs in a given direction in a given map repetition (or for a subset of those, in the very large COSMOS maps). The stacking result was then used to compute the average offset to be applied to this set of scan-legs, for a given direction, in a given map repetition. This procedure also implicitly corrects for small timing offsets between pointing information and data. Absolute, systematic astrometric offsets turned out to be as high as 5 arcsec, while relative corrections between individual submaps are approximately 1 arcsec.

Map reconstruction is done via simple image co-addition, based on a simplified version of the "drizzle" method (Fruchter & Hook 2002). Given the high data redundancy in the GOODS-N field, the drop size is set to 1/8 of the input array pixel size. This corresponds to 1/5 and ~1/4 of the output pixel size at 100 μm and 160 μm, respectively, thus reducing the correlated noise in the final map. Fields with lower redundancy were mapped by adopting a smaller drop size (1/4 of the input PACS array pixel size). Images produced from each observation were weighted according to the effective exposure of each pixel and co-added to produce the final maps. The final error map was computed as the standard deviation of the weighted mean. Owing to the nature of scan maps, correlations exist between nearby pixels, in particular along the scan direction. These correlations are close to uniform across the final map, thus we derived a mean correlation correction factor which was then accounted for in the errors on the extracted fluxes.

PACS catalogs were extracted following two different approaches, optimized for the different scientific aims of the PEP project. We performed a blind extraction using the Starfinder PSF-fitting code (Diolaiti et al. 2000) and a guided extraction using 24 μm priors, following the method described in Magnelli et al. (2009). The two methods provide similar results: fluxes extracted in the two cases are consistent with each other, the

[1] See the PEP web page for information about the other fields in the survey: http://www.mpe.mpg.de/ir/Research/PEP/.

[2] HCSS is a joint development by the *Herschel* Science Ground Segment Consortium, consisting of ESA, the NASA *Herschel* Science Center, and the HIFI, PACS and SPIRE consortia.

Table A.1. PEP fields: total exposure times, noise properties, flux levels for 80% completeness and 30% spurious fraction, statistics of *blind* catalogs, and results of maximum-likelihood match to the multi-wavelength ancillary catalogs (labeled "multi", GOODS-N only).

Field & band	Area	t_{exp} [h]	rms [mJy]	$N(PACS)$ $>3\sigma$	Compl. 80%	Spur. 30%
GOODS-N 100	$10' \times 15'$	30	1.00	291	5.5	2.5
GOODS-N 160	$10' \times 15'$	30	1.90	317	11.0	7.0
100+160	–	–	–	201	–	–
100+multi	–	–	–	254	–	–
160+multi	–	–	–	274	–	–
100+160+multi	–	–	–	187	–	–
100+multi+zspec	–	–	–	162	–	–
160+multi+zspec	–	–	–	169	–	–
100+160+multi+zspec	–	–	–	125	–	–
A2218 100	$4' \times 4'$	13	0.84	98	5.4	3.0
A2218 160	$4' \times 4'$	13	1.59	94	11.8	7.6
LH[a] 100	$24' \times 24'$	35	~1.3	~780	~7.0	~4.0
LH[a] 160	$24' \times 24'$	35	~2.7	~700	~14.5	~9.5
COSMOS[b] 100	$85' \times 85'$	182	~2.0	~5750	~9.5	~6.3
COSMOS[b] 160	$85' \times 85'$	182	~4.0	~4900	~20.5	~12.0

Notes. [(a)] The PEP Lockman Hole field is the ROSAT-HRI and XMM field. [(b)] COSMOS will reach 213 h of integration at full depth.

prior extraction leading to slightly deeper – although possibly biased – catalogs. The number counts presented in this paper were built on the blind catalog. Point spread function (PSF) profiles were extracted from the final science maps, and turn out to have an *FWHM* of ~7.5 and ~11 arcsec in the 100 μm and 160 μm bands, respectively. Aperture corrections were characterized on calibration observations of the Vesta asteroid. Absolute flux calibration is based on γDra, αTau, and αCMa and makes use of the standard calibration file embedded in the PACS pipeline (version 2.0.1328). Typical absolute flux calibration errors are ~10% and include uncertainties on instrumental characterization, PSFs, and reference stars analysis.

Noise in PACS maps was measured with random aperture extractions on residual images and compared to the observed S/N ratio for the detected sources. The rms values thus obtained include both instrumental noise and confusion noise due to undetected sources (i.e., below the 3σ threshold). This measured 1σ noise is 1.00 mJy at 100 μm and 1.90 mJy at 160 μm for GOODS-N. Table A.1 includes the noise properties of the SDP fields, as well as the Lockman Hole and COSMOS.

To quantify the reliability of extracted fluxes, the level of incompleteness and the fraction of spurious sources, Monte Carlo simulations were performed, creating 500 images and adding 20 artificial objects onto science maps each, for a total of 10 000 sources. Input and output fluxes are consistent with each other within a few percent. Completeness is defined as the fraction of sources that have been detected with a photometric accuracy of at least 50% (Papovich et al. 2004). Spurious sources are defined as those extracted above 3σ with an input flux lower than $3\sigma(Image)$. The latter is consistent with the spurious fraction inferred by blindly extracting from inverted maps. The GOODS-N blind catalog reaches 80% completeness at ~5.5 mJy and ~11.0 mJy in the two bands, and a 30% fraction of spurious detections at ~2.5 and ~7.0 mJy, in green and red respectively (see Table A.1).

The GOODS-N field benefits from an extensive multi-wavelength coverage. Adopting the Grazian et al. (2006) approach, the PEP Team built a reliable multi-wavelength, PSF-matched database, including ACS *bviz* (Giavalisco et al. 2004), Flamingos *JHK*[3] and *Spitzer* IRAC data. Moreover, MIPS 24 μm (Magnelli et al. 2009) and Barger et al. (2008) deep *U*, *K*s, and spectroscopic redshifts have been added. When no spectroscopic redshifts were available, photometric redshifts have been derived using the EAZY code (Brammer et al. 2008).

The 100 and 160 μm blind catalogs were finally linked to this multi-wavelength catalog through a three-band maximum likelihood procedure (Sutherland & Saunders 1992), starting from the longest wavelength available (160 μm, PACS) and progressively matching 100 μm (PACS) and 24 μm (*Spitzer*/MIPS) data. Table A.1 summarizes the main properties of blind catalogs, as well as the results of the maximum-likelihood match in GOODS-N.

Confusion is a major concern in deep wide-beam observations, like far-IR or sub-mm imaging of blank fields. PEP *Herschel* observations are not dispensed from confusion: the high density of detected sources hinders the extraction of fainter objects, in the so-called "source density confusion criterion" (SDC, Dole et al. 2003). Adopting the Lagache et al. (2003) definition of *beam* (i.e., $\Omega = 1.14 \times \theta^2_{FWHM}$), the source density in PACS blind catalogs is 40 beams/source at 100 μm and 18 beams/source at 160 μm. This indicates that PEP GOODS-N is already hitting the SDC limit in the PACS red band, estimated to be 16.7 beams/source by Dole et al. (2003), while the green channel is not affected. By extrapolating integral number counts, we estimate that this limit will be reached at ~2.0 mJy at 100 μm and ~4.7 mJy at 160 μm. Nevertheless, this limit is known to be rather conservative, and some authors have already shown that source extraction can be reliably carried out to levels as low as 10 beam/source under favorable conditions (e.g. at 24 μm, Magnelli et al. 2009).

[3] Kindly reduced by Kyoungsoo Lee.